Self-heating behavior during cyclic loadings of 316L stainless steel specimens manufactured or repaired by Directed Energy Deposition

Yanis Balit, Louis-Romain Joly, Fabien Szmytka, Sylvain Durbecq, Eric Charkaluk, Andrei Constantinescu

Self-heating behavior during cyclic loadings of 316L stainless steel specimens manufactured or repaired by Directed Energy Deposition[1]

Yanis Balit[a], Louis-Romain Joly[b], Fabien Szmytka[c], Sylvain Durbecq[a], Eric Charkaluk[a], Andrei Constantinescu[a]

[a] *Laboratoire de Mécanique des Solides - École Polytechnique, Institut Polytechnique de Paris, CRNS, 91128 Palaiseau, France*
[b] *Direction Innovation et Recherche - SNCF, 1 avenue François Mitterand, 93210 Saint-Denis, France*
[c] *Institute for Mechanical Science and Industrial Application - CNRS, EDF, CEA, ENSTA Paris, Institut Polytechnique de Paris, 828 Boulevard des Marechaux, 91762, Palaiseau, France*

Abstract

The purpose of this article is to assess a self-heating testing method for the characterization of fatigue properties of single-track thickness additively manufactured specimens. It also evaluates the impact of the microstructure orientation with respect to the loading direction on the dissipative behavior and the initiation of microcracks. The 316L stainless steel specimens under scrutiny were manufactured by Directed Energy Deposition in two configurations: (i) fully printed specimens (2 orientations) and (ii) repaired specimens. The paper first presents a morphologic and crystallographic texture analysis and second, a series of self-heating tests under cyclic loading. The microstructural analysis revealed elongated grains with their sizes, shapes and preferred orientations controlled by process parameters. The self-heating measurements under cyclic tensile loading proved that the dissipation estimation through infrared measurements can be performed on small scale, thin specimens. The self-heating curves could successfully be represented by the Munier model. Moreover, several links between the printing parameters and self-heating results could be established. For example, a smaller vertical increment between successively deposited layers leads to higher mean

[1] published in Materials Science & Engineering A 786 (2020) 139476

endurance limits in all configurations. Repaired specimens had a lower mean endurance limit when compared with fully printed or conventionally manufactured substrate specimens. Finally, anisotropy was highlighted during these cyclic tests: specimens loaded orthogonally to the printing direction (PD) showed higher fatigue limits when compared with the ones tested along the PD. Additionally, post-mortem observations revealed characteristic microcracking patterns initiated during the self-heating experiments. Loading along the printing direction induced a classical dominating crack, whereas orthogonal loading generated a network of microcracks along the printing direction. This suggests that the damage, such as void opening, where concentrated at the interlayers. Additionally these damage patterns can be correlated with patterns of plasticity at the grains scale observed in a previous study.

Keywords:
Directed Energy Deposition, Fatigue, Microstructure, Repair, Self-heating

---

1. Introduction

Traditional cladding processes for the repair of structures with an identical or a different material have been investigated in the past decades. For instance, arc welding [1], thermal/plasma spraying [2; 3; 4] and cold spray [5] have been studied extensively but their broad deployment has been prevented by severe limitations. In particular, these processes induced a large heat affected zone (HAZ), critical distortions, poor accuracy and poor mechanical properties without additional treatments. Directed Energy Deposition (DED), one of the two main metallic Additive Manufacturing (AM) technologies received particular attention as an alternative repairing technique in the past years. The DED technology is an additive manufacturing process, where the feed material is transported into a focused heat source and deposited on the previously constructed layers [6]. Particular variants of the DED process have been denoted in several ways in the literature as: Direct Metal Deposition (DMD), 3D laser cladding, Laser Metal Deposition (LMD) and Direct Laser Deposition (DLD) amongst others. One of the key advantages of the DED technology is the deposition ability on a non-planar substrate, which allows deposition of coatings [7] or to repair complex geometries [8; 9]. However, when it comes to accuracy or geometric complexity of the manufacturing parts, it does not reach the performances of Powder Bed Fusion (PBF), a complementary metallic AM technology [10].

Manufacturing or repairing with a DED technology requires the understanding of the intrinsic microstructure generated process and its effect on the mechanical properties. Several research groups investigated the effects of the process parameters such as laser power, powder flow, deposition speed etc. on additively manufactured parts and highlighted the presence of oriented microstructure with elongated grains as well as anisotropic macroscopic properties [11; 12; 13]. A discussion in [14] of the microstructure for a Vanadis 4 metallic substrate repaired by LMD with two different powders, CPM 10V and Vanadis 4, showed that the microstructure of the resulting repaired part was similar to a quenched alloy tool steel. Thus, it indicates that the technology is adapted for repair. With optimized parameters, DED can attenuate the HAZ, create metallurgical-bonded deposits, and reduce the distortion, i.e. it can solve the above mentioned problems [15; 16]. Therefore, it is particularly interesting for repairing high value components [17; 18].

For instance, a comparison of laser-cladding and gas metal arc welding of gray cast iron repair is presented in [19]. It revealed a larger heat affected

zone and shorter ultimate elongations for components repaired by gas metal arc welding. It highlights the superior properties for components repaired by laser-cladding. The repair both in terms of shape of the slot and in volume as well as the lasing strategy were found to be of high importance for the final properties of the repaired specimens. The polycrystalline microstructures of 316L stainless steel used for the repair of tools has been discussed in [20]. The study underlines a complex dendritic structure growth as a consequence of irregular nucleation. The simulation work focusing on repairs of different sizes by laser-cladding found that cracks occurred around the repair only for the deepest ones and explained their occurrence by the presence of thermal stresses and oxide inclusions. In [21], the authors noticed that a trapezoidal slot shape resulted in a porosity free bonding compared to results obtained with rectangular slot shape. In addition, the authors observed that the scanning strategy, particularly the diagonal pattern, had an influence on the friction coefficient and the wear resistance.

Another important aspect of additively manufactured metallic parts are the fatigue properties and lifetime predictions. These properties are assessed at the macroscopic scale of the structure. However, they depend on the plasticity mechanisms and the particular grain structures at the microscopic scale of the material as discussed for example in [22; 23]. Fatigue life in as-built AM metallic materials has been assessed and discussed under different settings: the influence of processing conditions and the resulting defect structure is highlighted in [24; 25], and the role of the particular microstructure has been underscored by exhibiting anisotropy properties for static and cyclic loadings in [26; 12] and [25; 27], respectively. More precisely, a study in [25] focused on Direct Metal Laser Sintering of 316L stainless steel found that the measured fatigue strength was close to the value measured for wrought material when subjected to uniaxial stress parallel to the printed layers. However, when the loading direction was perpendicular to the printed layers, fatigue fractures occurred prematurely by separation of the material. In the case of a 304L stainless steel manufactured by DED [27], an improvement of the fatigue properties of the printed material was reported. More precisely, for a loading acting perpendicularly to layers, the fatigue limit was 25% superior in the 10^4-10^6 cycle range and performed identically in the high cycle fatigue regime when compared with wrought material. In the high cycle fatigue regime, a 7% decrease of the fatigue limit was measured for loadings parallel to the layers when again compared to the wrought material.

The fatigue properties of DED repaired structures are for now less investi-

gated. In [28], the authors reported that the repair of an AISI 4340 substrate with the same material presented poor tensile properties and a significantly reduced fatigue life. Nevertheless, the replacement of the cladded layer with an AerMet 100 steel improved the fatigue life by a factor 10. Additionally, the authors noticed that a heat treatment improved the fatigue limit slightly above the limit of a grind-out substrate. Repair strategies by DED for Ti-6Al-4V specimens and the effect of an inter-track pause were reported in [29]. A clear difference of microstructure and a 50% larger tensile residual stress was observed for the specimen manufactured with an inter-track pause. For the latter, the measured fatigue life was shorter and attributed to geometrical defects.

These studies equally highlight the difficulties and the underlying cost of providing a large data-base of fatigue properties that can largely vary with process parameters. Therefore, alternative and faster methods are required to determine such properties.

One of the rapid methods for the investigation of fatigue properties is based on the self-heating of the specimen due to microscopic plasticity generating damage under cyclic loadings. The technique was initially proposed by Stromeyer in 1914 [30] for a rapid determination of the mean fatigue limit defined in this context as the minimum level of alternating stress which will induce heat in the tested specimen. Over the years, this method was refined and applied to various materials and configurations [31; 32; 33; 34; 35; 36; 37]. In [38], the authors proposed a two scale probabilistic model based on two dissipative mechanisms, corresponding to the primary and secondary dissipation regime to analyze the self-heating phenomenon. To our knowledge, this method has not been yet used to analyze the fatigue of repaired parts by DED. More generally, the method enables a fast determination of fatigue properties in AM parts which opens up the possibility of an extended parametric analysis.

The objective of this paper is to assess the damage evolution for single-track thickness specimens using the self-heating testing method and to evaluate the method for thin, small scale, fully printed and repaired specimens. The results will equally prove that the difficulties of thermographic measurements on small scale specimens can be overcome.

The article starts with the presentation of the specimens and the experimental techniques. It then discusses the characterization of the microstructure and exhibits the macroscopic mechanical properties during uniaxial tensile tests. Next, the article analyses and discusses measurements of the self-

heating phenomenon during increasing cyclic loadings and finishes with several concluding remarks.

2. Materials and Experiments

2.1. Manufacturing of the specimens

A series of single-track thickness walls were built by Directed Energy Deposition (DED) in two configurations as shown in Figure 1. First, a set of $100\,mm \times 30\,mm \times 0.7\,mm$ walls was printed on a horizontal 316L stainless steel substrate, on which fully printed specimens were extracted in two orientations with respect to the printing direction. A second set of $50\,mm \times 15\,mm \times 0.7\,mm$ walls was printed on a vertical substrate in which "repaired" specimens being half substrate half printed were extracted. For both configurations, the specimens were extracted at the center of the walls by water jet cutting with a *Mach 2b water jet* [39]. Two orientations of the fully printed specimens enable the application of a perpendicular or parallel tensile loading with respect to the printing direction.

The precise shape of the dogbone specimens does not follow shapes of classical experimental standards but was imposed by local experimental constraints, i.e. the size of the ion polisher chamber, the shape of the fixtures of the in-situ SEM tensile machine, etc. The homogeneity of the macroscopic stress distribution in the zone of interest was verified using a finite element analysis prior to the start of experiments.

The shorter length of the repaired walls was dictated by practical experimental limitations. Moreover, a different printing length of the layers imposes, with the same process parameters, a different thermal history. It consequently results in different microstructures and residual stresses as reported in [29]. To avoid this effect, we added a dwell time of $1\,s$ between two consecutive layers in order to compensate for the length ratio of 2 for the fully printed and repaired walls. As a consequence, the similar thermal history at the center of the wall replicated the microstructure. Let us further mention, that additional parameters such as the difference of size of the substrates and their effect on the heat conductivity and capacity of the system were not quantified in this study.

The metallic powder used in this study was a 316L stainless steel from Höganäs AB [40] generated by gas atomization with a particle size in the range of 45-90 μm. This material was chosen in this study for its weldability and mechanical properties. For both configurations, walls were printed with the following parameters of the machine: (i) a powder flow of $6.5\,g/min$, (ii) a deposition speed of $2000\,mm/min$ and (iii) a laser power of $225\,W$. Additional information concerning the powder, the additive manufacturing

machine Mobile from BeAM [41] as well as the process calibration are available in previous studies [11; 42]. Also, a back and forth printing strategy along the printing direction (PD) was employed for the manufacturing as shown in Figure 1. For both configurations, the effect of process parameters on the microstructure and mechanical behavior was studied through the effect of two different vertical increments i.e. the vertical spacing between the successive deposited layers. For both vertical increments, i.e. $0.12\,mm$ and $0.2\,mm$, the targeted final dimensions of the walls were reached. This indicates that both vertical increments are suitable for repair. However, the precise value of the vertical increment imposes a specific thermal history. More precisely, a ratio of 5/3 between the number of back and forth scans for the $0.12\,mm$ and $0.2\,mm$ vertical increments was necessary in order to reach the same final height of the wall. Consequently, different properties and microstructures were generated for the two vertical increments as presented and discussed next.

We shall denote the specimens manufactured with a vertical increment of $0.12\,mm$ and a perpendicular or parallel tensile direction to the PD as $A_{\perp\,0.12}$ and $B_{/\!/\,0.12}$ respectively, as represented in Figure 1. For a vertical increment of $0.2\,mm$, they are denoted as $A_{\perp\,0.2}$ and $B_{/\!/\,0.2}$ respectively. Finally, the repaired specimens manufactured with a vertical spacing of $0.12\,mm$ and $0.2\,mm$ are named $R_{0.12}$ and $R_{0.2}$ respectively and their dimensions in mm (common to the fully printed ones) are shown in Figure 1.

2.2. Specimen preparation and observation

The specimens were mechanically polished after extraction from the wall. The final mirror surface, needed for Electron Backscatter Diffraction (EBSD) maps acquisition, was reached after an additional ion polishing. The precise procedure and parameters are available in [11]. Moreover, the surface polishing eliminated the natural surface roughness created during the DED process and the eventual initiation sites of surface defect. Indeed, in [20], it was noticed that the fatigue properties of Ti-6Al-4V samples, produced by direct metal laser sintering and electron beam melting, are dominated by surface roughness. The effect would have been particularly important as the roughness in comparison to the specimen thickness is high for single-track thickness specimens.

The microstructure was analyzed qualitatively and quantitatively in terms of grain size, shape and distribution from the data of the EBSD map. In order to control the microstructure and measure precisely the influence of the

vertical spacing between layers, we paid close attention to the following conditions: (i) extraction of the specimens in the middle and at the same height of the wall (ii) introduction of a dwell time for the repaired specimens, (iii) precise control of the level of polishing, implying similar thicknesses for the final specimens, (iv) acquisition of the EBSD maps with a step size of 1 μm. The conditions ensured a consistent material control and specimen preparation, but also a large data-base that contains a statistically representative number of grains.

In order to simplify the discussion and avoid redundancy, only the following configurations will be reported next: $A_{\perp\,0.12}$, $B_{/\!/\,0.2}$, $R_{0.12}$, $R_{0.2}$.

2.3. Mechanical testing

Tensile tests were conducted under quasi-static monotonic loading on an electro-mechanical *Instron ElectroPulsTM E3000* machine [43]. The tests were performed using a $3\,kN$ load cell at a fixed strain rate of $2.10^{-2}\,s^{-1}$. The strain field was obtained by Digital Image Correlation (DIC) using the software *Correlation Manual Value* (CMV) [44; 45] on a coarse speckle created with black and white paints.

For the self-heating experiments, specimens were painted using black paint to ensure an emissivity close to 1. Moreover, to limit the thermal noise from the surroundings, the complete experimental set up was insulated by a protective enclosure, see Figure 2 for details.

Self-heating tests were performed using the same *Instron* machine. The loading protocol consists of applying a successive series of blocks of cycles which gradually increase in terms of stress amplitude Σ_0 while keeping a constant loading ratio $R_\Sigma = 0.1$. R_Σ is defined for each block of cycles as follows:

$$R_\Sigma = \frac{\sigma_{min}}{\sigma_{max}} \tag{1}$$

with σ_{min} and σ_{max} referring to the minimum and the maximum stress, respectively (see Figure 3(a)). The positive value of $R_\Sigma = 0.1$ avoids compressive loads and prevents the buckling of the thin specimens. The specimens were tested at the frequency of 30 Hz for 20000 cycles per block. For each printed configuration, the tests were performed twice.

Thermal measurements have been carried out using the *FLIR X6580sc* camera [46] at the recording frequency of 10 Hz. The camera was focused on

the specimen's surface using a G1 lens allowing a resolution of $15\,\mu m/pixel$ on a $3 \times 4\,mm^2$ area.

Local heat increase, recorded for each block of cycles, is a consequence of the energy dissipation due to irreversible phenomena at the microscopic scale: microplasticity, microcraking, etc. More precisely, the temperature elevation for a block of cycles is defined as the difference between the average temperature recorded during the block of cycles and the average temperature attained in the break between two successive blocks. Indeed, the 3 minutes break permits the dissipation of the accumulated heat during the cycles of the preceding block. The data corresponding to the temperature elevation with respect of the stress amplitude are plotted in Figure 3(b).

The measurement of the heat increase is a delicate task in the case of thin specimens and small quantities of dissipated energy due to multiple sources of heat loss. Heat loss by conduction arises at the jaws fixing the specimen and by convection with the surrounding air. A prior article of self-heating tests [38], reports for example that hot oil circulating in the hydraulic press increases temperature of the jaws and consequently the specimen. The machine used in the present case was oil-free and based on a linear motor technology. Therefore, it enabled us to focus on the variation of the specimen's temperature due to the microscopic plasticity during the cyclic loadings.

Let us further remark that the temperature increases with the stress and falls into two distinctive regimes as shown in Figure 3(b). The primary regime corresponds to a small limited dissipation regime with almost vanishing heat increase. In contrast, the secondary regime exhibits an important elevation of temperature with increasing amplitudes of stress. The stress amplitude Σ_0 marking the change of regime, is associated with the fatigue limit characterizing infinite lifetime, as discussed in [47; 48]. The measured results for all our configurations were interpreted using Munier's model [38], which was fit to the data using a least-square method.

3. Result and discussion

3.1. Microstructure

To reiterate, to simplify the discussion only the following configurations will be reported in this section:$A_{\perp\,0.12}$, $B_{/\!/\,0.2}$, $R_{0.12}$, $R_{0.2}$.

Typical microstructures of fully printed or repaired specimens with a vertical increment of $0.2\,mm$ are presented in Figures 4 and 5, respectively. On these two EBSD maps corresponding to the microstructure of the specimen $B_{/\!/\,0.2}$ and $R_{0.2}$, one can observe similarities in term of morphological aspects. Moreover, orientation of grains exhibits a clear ziz-zag pattern, which corresponds to the deposition direction during the back and forth scanning of the laser. A zoom image of both microstructures is displayed on the same figures. It can be noticed that printing layers are recognizable by the underlying grain pattern. Furthermore, the printed layers are composed mainly of large grains, while isolated clusters of small grains are located at the interlayers. To the best of our knowledge, the precise formation of the small grains is still unknown and currently under investigation. Observations with a thermal camera suggest that the clusters of *small* grains are not related to a lack of fusion at the interlayers as several layers are reheated by each passage of the laser.

Grains were statistically analyzed in terms of morphology, i.e. shape, surface, orientation, etc. For convenience, they were sorted into two families with respect to their equivalent grain diameters, i.e. *small* and *large* grains. The threshold value between the two families of grains is $15\,\mu m$ and corresponds to the equivalent diameter of a disk matching by surface the biggest grain found in a cluster of *small* grains.

In the case of the fully printed or repaired specimens with a vertical increment of $0.12\,mm$ (see Figure 6 and 7 respectively), one can remark that the deposited layers are less recognizable. Furthermore, clusters of small grains are absent even though *small* grains are still present (detailed later).

The shape of the grain will be characterized by the aspect ratio, defined as the ratio of principal axes of the smallest circumscribed ellipse. Therefore an aspect ratio of 1 indicates an equiaxed grain. For all specimens, the distribution of the grain sizes and shapes can be described by the probability density function (PDF) in terms of the equivalent grain diameter and of the aspect ratio, as illustated in Figure 8. The main statistical features of the

shape and size data such as the equivalent diameter average, aspect ratio median etc. are summarized in table 1.

The analysis of the comparative plot of the equivalent grain diameter distributions displayed in Figure 8(a) is pointing out the influence of the vertical increment for the fully printed specimens. In this plot, the $0.12\,mm$ and $0.2\,mm$ vertical increments are represented by $A_{\perp\,0.12}$ in blue and $B_{/\!/\,0.2}$ in red respectively. The continuous, dashed and dotted lines illustrate the data of the whole EBSD map, the *large* grains and the *small* grains respectively. One can remark that the distribution corresponding to all grains is more spread for $A_{\perp\,0.12}$ than for $B_{/\!/\,0.2}$ with an average equivalent grain diameter of $26.8\mu m \pm 20.8\mu m$ (median of $22\mu m$) and $14.7\mu m \pm 14\mu m$ (median of $9\mu m$), respectively. A focus on the two families of grains previously presented shows that for $A_{\perp\,0.12}$, the distribution for *large* grains is more spread with a higher equivalent diameter of $35.2\mu m \pm 19.3\mu m$ and a spread expressed by a median of $29.9\mu m$ than for $B_{/\!/\,0.2}$ which has an equivalent diameter of $29.6\mu m \pm 15.3\mu m$ and a median value of $24.4\mu m$. The same scrutiny for the *small* grains shows similar distribution trends with a slight offset for their respective peaks. Same as for the *large* grains, the *small* ones shows higher equivalent diameter of $8.9\mu m \pm 3.6\mu m$ (median of $9.9\mu m$) for $A_{\perp\,0.12}$ than for $B_{/\!/\,0.2}$ which has an equivalent diameter of $7.2\mu m \pm 3.4\mu m$ (median of $6.5\mu m$). Also one can note that for the specimens $A_{\perp\,0.12}$, the *small* grains represent 32.7% of the microstructure although occupying 10.5% of the surface while for the specimen $B_{/\!/\,0.2}$, they represent 65.6% of the microstructure despite occupying 31.4% of the surface. A similar trend is observed for the equivalent grain diameter of the specimens $R_{0.12}$ and $R_{0.2}$ on figure 8(c).

Figure 8(b) portrays the distribution of the aspect ratio of the grains of the fully printed specimens. For the grains in specimen $B_{/\!/\,0.2}$ represented by the blue lines, the aspect ratio curves present distinct PDF for the two families of grains. *Large* grains have a wide distribution of the aspect ratio with an average of 3.3 ± 2 (median of 2.8). *Small* grains present a narrow distribution of the aspect ratio with an average of 2.4 ± 1.4 (median of 2). Grains in specimen $A_{\perp\,0.12}$, represented by the red line, manifest a similar trend. The average values of the aspect ratio are now 2.4 ± 1.2 (median of 2.1) and 2.3 ± 1.3 (median of 2) for the *large* and *small* grains, respectively.

The microstructural texture, in terms of both morphology and crystallographic orientations is determined by the local heat flow during solidification and cooling[49; 50; 51]. The cooling history and the orientation of the thermal gradient will impose the preferred growth directions of the grains and fix

their orientation observed previously in the zig-zag pattern. More precisely, the particular heat flow pattern depends on the geometry of the specimen and the substrate, the conduction and heat exchange coefficient as well as the heat input defined by the printing parameters. These parameters are the power of the laser, the printing speed, the scanning pattern strategy etc. In our case, an additional parameter, the vertical increment, is equally driving the position of the heat source in the transient heat flow problem. For the $0.2\,mm$ specimens, the zig-zag pattern is inherited from the thermal gradient and flow during the printing as also reported by [49]. Manufacturing with a smaller vertical increment of $0.12\,mm$ imposes a larger local heat during the manufacturing of the successive layers. In this case, the thermal gradient and flow are less influenced by each laser passage. Overall, one could simplify the reasoning by stating that the grain size is proportional to the heat energy absorbed from the laser and that the shape and orientation are driven by the cooling rate and direction. We recall our previous observation: the wall with a $0.12\,mm$ vertical increment requires 5/3 times more back and forth passages than the wall with a $0.2\,mm$ vertical spacing. This implies almost twice as much laser energy and subsequently more heat in the manufactured wall. This could explain the global difference in size of the grains as well as the lower volume fraction of *small* grains.

Finally, one can conclude that: (i) a clear zig-zag pattern is distinguished for the $0.2\,mm$ vertical increment and an absence of pattern for $0.12\,mm$ vertical increment, (ii) *large* grains are columnar, whereas *small* ones are equiaxed, (iii) the separation of aspect ratios between *small* and *large* grains is more pronounced in the case of the $0.2\,mm$ vertical spacing than in the $0.12\,mm$ scase.

Figure 9 exhibits the crystallographic texture as the pole figure of the crystallographic family of planes {100} for fully printed and repaired specimens with respect to the two vertical increments. Building and printing directions denoted as BD and PD respectively, are indicated with arrows in the diagrams. Well known results from solidification theory, see for example [52], state that the growing directions in the crystal are chosen among the directions involving the smallest number of atoms. As a consequence, the face-centered cubic (FCC) 316L steel of this study presents a preferred growth in the <001> direction. Additional remarks can also be found in [53; 54].

In the case of the configuration with a $0.2\,mm$ vertical increment, one can notice for both fully printed and repaired specimens, the presence of similar

textures with two maximal values, i.e. the red hotspots on the horizontal axis. The texture is the representation of the complete specimen and therefore includes the layers printed from left-to-right and the layers manufactured from right-to-left. These two layer families are responsible for each one of the two hotspots. Therefore, the crystallographic texture can be expressed as the sum of two fiber textures.

From the graph, one can read that the angle between the vertical BD axis and each of the hotspots corresponds to a tilt angle of $\approx \pm 30°$. The angle agrees with previous morphological measurements, i.e. the orientation of the larger axis of the equivalent ellipse. Let us further mention that the angle is an indirect measure of the maximum heat flow during cooling, as discussed in [51].

The configuration with a $0.12\,mm$ vertical increment shows different preferred orientations as presented in Figure 9. One can recognize for the fully printed specimen, a fiber texture pointing to the outer wall surface with a tilt half way between the Normal Direction (ND) and the PD.

Let us recall that the heat accumulation is larger in this case as the printing nozzle had to do 5/3 times the number of passages in comparison to the $0.2\,mm$ wall. Moreover, the crystallographic texture orientation is dependent of the heat flow direction. The tilt toward the normal of the outer wall indicates that for this configuration, the gradient of the thermal flow is tilted towards the outer surface. It therefore illustrates an important increase of the cooling through convection with the outer surface and a proportional smaller importance of the cooling mechanism by thermal conduction through the substrate and previously deposited layers.

Last but not least, in contrast to the configuration with a vertical increment of $0.2\,mm$ where the fully printed and repaired specimens have the same crystallographic texture, a different preferred orientation are observable for fully printed and repaired specimens with vertical increment of $0.12\,mm$. In the case of the repaired specimen, the texture indicates a tilt of the $\{100\}$ direction from the building direction axis toward the Normal Direction and a rotation along a vector aligned with the Normal Direction. This particular texture is obtained near the repaired interface, where texture of the substrate is thought to influence the preferred growth orientation of the grains. One can expect that the texture should evolve toward the pattern observed for the fully printed specimen with a surface of study further from the interface. However, the distance from the interface for which the preferred orientation of $R_{0.12}$ evolves to the crystallographic texture of $A_{\perp\,0.12}$ was not found in

this study suggesting that the difference in conduction through the substrate was not equalized.

To sum up, changing the vertical spacing between printed layers affects thermal time and space distribution and, therefore yields differences in crystallographic textures. More precisely, we found that for the fully printed and repaired specimens with a vertical spacing of $0.2\,mm$, the texture is to be associated with the back-and-forth printing strategy and the ensuing heat flow pattern. Reducing the vertical spacing between layers increases the retained heat present in the wall. However, the conductive cooling by the substrate is not able to accommodate the heat increase. Consequently, the relative importance of the convective cooling at the surface increases, which modifies the direction of the temperature flow gradient Further investigations to quantify the observations are underway.

3.2. Tensile properties

For both vertical increments, 3 monotonic tests were performed for the repaired and fully printed specimens in order to determine their respective mechanical properties. In order to facilitate a quantitative comparison of the tensile properties, we provide standard material parameters such as the yield stress (σ_y), ultimate tensile strength (UTS) and the ductility (D). Moreover, we introduce as a characteristic of the anisotropy, the ratio, $r_{/\!//\perp}$ of each material parameters. The ratio compares the values obtained from the tests parallel to the printing direction with the value obtained for the tests perpendicular to the printing direction. Moreover, the data is compared to data extracted from literature [12; 26; 55]. A global view is proposed in table 2.

One can remark that the ductility is almost similar for the specimen $A_{\perp\,0.2}$ and $B_{/\!/\,0.2}$ with a ratio of 0.98, indicating an isotropy of this property. However higher ratio values of 1.14 and 1.15 are observable for the yield and ultimate strength respectively, indicating an anisotropy of these properties. For $A_{\perp\,0.12}$ and $B_{/\!/\,0.12}$, similar trends can also be noticed for the yield and the ultimate strength, with ratios of 1.06 and 1.05 respectively, indicating a weaker anisotropy than before. Previous publications on stainless steel employing DED as a manufacturing technology presented similar results regarding the mechanical behavior under uniaxial tensile test [26; 56; 57; 12; 55]. Higher σ_y and UTS for the specimens parallel to the PD were found as shown in table 2. However, in these cases, specimens tested perpendicularly to the PD had higher ductility while in this study, the ductility was found almost similar for both orientations. The difference in geometry of the specimens can explain

this difference but this aspect was not investigated. The particular elongated microstructure induced by this additive manufacturing process is at the origin of this particular anisotropy. Indeed, grains are columnar i.e. depending on the tensile orientation, dislocations meet more or less boundaries resulting in a difference in properties [58]. Also, a less marked anisotropy measured for the smaller vertical increment is thought to be due to a less columnar microstructure than for the $0.2\,mm$ configuration as demonstrated earlier.

Finally, one can remark that even though the trends are similar, the intrinsic values are spread as also summarized in [59]. The scattering of the mechanical properties are directly related to the different machines, geometry of the specimens, process parameters and material composition used in studies, see comments and discussion in [59; 60; 61]. Our work highlighted the difference of properties induced due to the variation of the vertical increment.

The corresponding tensile engineering stress versus strain curve of all the specimens tested in this study are plotted in Figure 10. One can remark in this Figure that the tensile strength of the repaired specimens falls between those of the substrate and $A_{\perp}$ ones for their respective vertical increment. In addition, the ductility is more limited than the two joined materials tested separately and these results were also shared by [62; 63]. An improvement of the properties by reducing the vertical increment is still present for the repaired specimens as exhibited for the fully printed specimens $A_{\perp\,0.12}$. Finally, all the repaired specimens fractured in the printed parted, far away from the interface, which indicates that the bonding zone is not a limiting weak zone during uniaxial static loadings.

3.3. Comparison of the self-heating curves

The self-heating test highlights two operating regimes of the material behavior by expressing the temperature elevation in the sample as a function of the applied stress's amplitude. In the first regime for small stress amplitudes, the temperature increase is negligible as a consequence of small mechanical dissipation. This is the signature of an elastic response at all material scales and an infinite fatigue lifetime. In the second regime at larger stress amplitudes, the temperature increase is noticeable and the consequence of a lack of mechanical dissipation due to irreversible mechanisms. The change between the two operating regimes is clearly marked by a threshold of the stress amplitude which is related to the fatigue endurance limit. The limit

is usually identified by the intersections of the linear approximations for the two operating regimes, or by the intersection of the linear regression of the three last points of the secondary regime with the stress amplitude axis as shown in [64; 65; 66]. The results have proven that the intersection matches the fatigue endurance limit at approximately two million of cycles. This fact was further verified in [38] for several steel grades with various microstructures. The comparison between the mean fatigue endurance limit obtained from self-heating measurements with a standard stair-case method showed an average error of less than 2%.

The success of a self-heating experiment is associated to the capacity to precisely measure the thermal dissipation due to the microscopic plasticity. The precision of thermal measurements increases with thermal inertia and results in a reliable determination of the endurance limit. The small and thin specimens of the single-track wall of this study place the samples in the region of small thermal inertia and challenging temperature measurements. As discussed in the materials section, part of the problem was tackled by the choice of the testing machine and by verification of the temperature distribution on the sample. However the acquired data proved to have an inherent scatter, which renders the determination of the fatigue limit using linear regression and line intersection unreliable. To overcome this difficulty, we propose to use the analytical model developed in [38] to relate fatigue data with the representation measured during the self-heating experiments. The model covers the complete data spectrum over the two operating regimes and therefore acts as a normalizing filter in the data determination.

The model is based on an energy balance and represents the temperature elevation as the sum of two contributions related to the two operating regimes. The temperature elevation Ω is defined as:

$$\Omega = \alpha(\frac{\Sigma_0}{\Sigma_{max}})^2 + \gamma(\frac{\Sigma_0}{\Sigma_{max}})^{m+2} \tag{2}$$

It is a function of the maximal stress amplitude before failure Σ_{max} and the stress amplitude per block Σ_0. These quantities are supposed to be known from experimental data. α, γ and m are real numbers and considered model parameters. α and γ have a physical meaning and are related to heat dissipation in the two operating regimes. Therfore, there are strictly positive. α, γ and m have been obtained by applying a linear regression to the experimental data.

The comparison between the identified model and the experimental data are represented for all tested configurations in Figure 11. Moreover, we have equally represented the linear tangent estimation of the secondary operating regime, which permits to obtain a rough estimation of the mean fatigue endurance limit at its intersection with the horizontal axis. The coefficients of the model and the mean endurance limits are listed in table 3.

The analysis of the parameter values reveals several aspects. The parameter α, describing the primary operating regime, a is zero value for most of the configurations and described correctly the measurement points lying on the horizontal axis. In contrast, the values obtained in [38] are higher and lie between 0.4 and 4.54. This difference is a consequence of the limited volume of our specimens.

Let us further notice that during the first loading blocks with low stress amplitude, the thermography camera could not capture any heat on the specimen. This means the dissipation required to offset the heat generated as a result of the microscopic plasticity was completely accounted for convection and conduction heat losses. Nevertheless, one can further remark that the model and the tangent lines produced coherent data and reasonable values for the mean fatigue endurance limits Σ_∞. More precisely, the mean endurance limits found for each specimen are lower than their respective yield strengths, i.e. Σ_∞ lies between 0.6- 0.8 of the yield strength, a magnitude that is be expected for a 316L stainless steel. Moreover the experimental scatter was controlled by the identification method.

Let us dive a step deeper in the data and analyze the effect of the DED process and manufacturing parameters on the self-heating behavior and more precisely on the limit Σ_∞. The comparison of the materials fabricated with vertical increments of $0.2\,mm$ and $0.12\,mm$ are represented by the ratio $r_{\Sigma_\infty \frac{0.12}{0.2}}$ of the respective limits, listed in table 4. One can notice that specimens with a smaller vertical increment, i.e. $0.12\,mm$ specimens, always exhibit higher fatigue limit with an improvement of 8%, 6% and 13% for the configuration $A_\perp$, $B_{/\!/}$ and R respectively. The improvement of the fatigue behavior was expected for $A_\perp$ and R, as these samples exhibited equally higher material values during monotonic tests. Overall, repaired specimens showed the lowest mean endurance limit in comparison to those of the substrate with a decrease of 11% and 21% for the $0.12\,mm$ and $0.2\,mm$ repaired configurations respectively.

Let us denote the ratio of the mean endurance limit of the specimens

tested perpendicular and parallel to the printing direction as $r_{\Sigma_\infty \frac{\perp}{/\!/}}$. As detailed in table 4, one can notice that specimens fully printed and tested perpendicularly to the printing direction have a higher Σ_∞ than the parallel specimens. This anisotropy was also shared in [55] and [27] in the case of 304L manufactured by DED and WAAM respectively. A similar trend was also presented in [67] for a 316L stainless steel printed by SLM. This is a stark reminder that mechanical anisotropy is very apparent during uniaxial tensile test for additively manufactured specimens. In fact, the specimens tested perpendicularly to the printing direction exhibit lower σ_y and UTS than the specimen tested along the PD [12; 26]. Anisotropy is also present during cyclic tests but in this case, perpendicular configuration shows higher fatigue limits than parallel one [55; 27] i.e the orientation effects are inverted for cyclic tests compared to the tensile ones.

This favorable orientation in terms of $r_{\Sigma_\infty \frac{\perp}{/\!/}}$ was quantified at 10% for the $0.12\,mm$ configuration and 8% for the $0.2\,mm$ configuration. These values are in the same magnitude as the ones found in the literature. The reason for this anisotropic behavior is explained in [68] as the consequence of the particular microstructure obtained by additive manufacturing. More exactly, the difference observed for the two orientations is associated with the presence of long grains oriented along the building direction. This microstructure induces a crack growth with a tortuous path in the case of a test perpendicular to the printing direction. In contrast, a more forward and less tortuous crack path with fatigue cracks predominantly growing along grain boundaries was noticed in the case of a specimen tested along the printing direction. In addition to the highly tortuous crack observed in the case of a perpendicular specimens, local mixed-mode fracture was also highlighted with the crack path often changing directions[69]. Therefore, these explanations could be a key to understand the anisotropy highlighted during cyclic tests, and the mechanism conducting to a favorable perpendicular configuration.

However during self-heating tests, the cyclic loadings are performed at lower stresses than the yield stress for a limited number of cycles per block. Therefore mostly microscopic plasticity phenomena are generated [38] rather than crack growth. Post mortem SEM images of specimens $A_\perp$ and $B_{/\!/}$ after the self-heating test are shown in Figure 12(a) and (b) respectively. For these 2 images, the printed layers are vertical for $A_\perp$ and horizontal for $B_{/\!/}$ i.e. the loading direction is perpendicular and parallel to the printing direction for $A_\perp$and $B_{/\!/}$ respectively. One can notice in (a) the presence of

multiple vertical cracks, while in (b) only two large cracks are present with one being responsible for the failure of the specimen. For both specimens, the cracks initiated at the highest stress i.e. during the last blocks.

In addition, these two post mortem images were investigated under the scope of the distribution of the crack sites. Therefore, images were cropped to the white frame (see Figure 12) and adjusted in order to have black pixels exclusively in the crack sites. One can observe the distribution of the black pixels for $A_{\perp}$ and $B_{/\!/}$ above their respective post mortem images in Figure 12(a) and (b). In addition, a gaussian filter was applied to smooth and clarify the trends. For the specimen $A_{\perp}$, one can notice the recurrence of the gaussian filter peaks to a distance corresponding to 2-4 layers. The opposite trend is noticeable for specimen $B_{/\!/}$. Indeed, except for the two large cracks, no peaks are observable. Therefore one can conclude different crack growth/failure mechanisms for both specimens. Next a comparison with strain localisation during monotonic tensile test of these specimens is shown in order to understand the two post mortem images.The complete procedure for obtaining a high resolution (full) strain fields and overlapping them on microstructural maps is available in [11]. In Figure 13, one can see that for specimen $A_{\perp}$, the strain localization is heterogeneously distributed between interlayers, while for the $B_{/\!/}$ the deformation is more homogeneously distributed. In addition in [11], it was observed that for $A_{\perp}$ clusters of small grains were present at interlayers and deformed less. Therefore, explaining why some interlayers are not localizing in terms of deformation. This result is thought to be a Hall-Petch effect. Moreover, it was observed that the strain localization is the same at low or high macroscopic deformation with only the magnitude of the strain evolving. For specimen $B_{/\!/}$, the authors found that the strain localisation was located in particular large grains. Finally by taking into account the microplasticity observations during monotonic tensile test, the self-heating behavior, and the final microcracks observations, it suggests that the microdamage mechanisms are different for the specimens $A_{\perp}$ and $B_{/\!/}$. One can propose the following scenario. A tensile load perpendicular to the printing direction, specimen $A_{\perp}$, will initiate a large number of extended dissipation zones located at intense plastic sites i.e. interlayers. Afterwards, these zones of high strain localization will generate a network of microcracks. Additionally, a crack shielding mechanism as proposed in [70] could also account for the network of cracks observed for $A_{\perp}$. In contrat, for specimen $B_{/\!/}$, a more classical fatigue scenario happens. One of the grain will generate localized plasticity. Afterwards, a large crack will initiate from this grain and

will continue until the specimen fails.
Therefore, extended dissipation zones at the interlayers for $A_{\perp}$ and a localized dissipation for $B_{/\!/}$ can explain why the transition between the primary regime and secondary regime happens at a higher stress amplitude for $A_{\perp}$. Further works are needed to validate such scenarios.

4. Conclusion

In this study, we investigated the self-heating behavior during cyclic loadings of 316L stainless steel specimens manufactured or repaired by DED. Specimens were extracted from bidirectionally-printed single-track thickness walls in different orientations and configurations.

We investigated the microstructure of the different printing configurations and unveiled their morphology and crystallographical texture. Results showed that modifying the vertical increment, i.e. one of the main process parameters, from $0.2\,mm$ to $0.12\,mm$ had a strong effect on the microstructure. The morphological texture presented a noticeable zig-zag pattern for the $0.2\,mm$ vertical increment and less perceivable one for $0.12\,mm$. Micrographs revealed that *large* grains have more distinguishable columnar shape than the *small* ones. The difference of the aspect ratio's of *small* and *large* grains is larger for the $0.2\,mm$ vertical spacing than for the $0.12\,mm$. Moreover, the results proved that the vertical increment affects the crystallographic texture in terms of a preferred grain orientation. We found that for the fully printed and repaired specimens with a vertical spacing of $0.2\,mm$, the texture can be associated with the back-and-forth printing strategy. For a $0.12\,mm$ vertical increment, the texture is different in the case of repaired and fully printed specimens. This difference has been associated with the influence of the substrate as a thermal reservoir and the heat accumulation in the wall once a certain height has been reached.

We explored the mechanical properties of the printed walls under monotonic tensile tests. An anisotropic behavior has been detected for the fully printed specimens. The specimens loaded along the printing direction, $B_{/\!/}$, exhibited higher mechanical properties in terms of yield strength (σ_y) and ultimate tensile strength (UTS) than specimen loaded perpendicular to the printing directions, $A_{\perp}$. The tensile strength of the repaired specimens is located between the strength of the substrate and fully printed specimen loaded perpendicular to the printed direction, $A_{\perp}$.

Self-heating tests yielded estimates of the fatigue endurance limit for the material. The specimens with a vertical increment of $0.12\,mm$ always showed a higher fatigue limit with an improvement of 8%, 6% and 13% relative to the configurations $A_{\perp}$, $B_{/\!/}$ and R, respectively. In addition, repaired specimens had a $\approx 11 - 21\%$ lower mean endurance limit compared to the substrate, manufactured by standard process. An anisotropic behavior was also discovered during these cyclic tests. Specimens loaded perpendicularly to the

printing direction showed higher fatigue limits ($\approx 8 - 10\%$) comparared to the ones tested along the printing direction. Post mortem analysis revealed a multitude of cracks at the interlayers for the specimens tested perpendicularly to the printing direction creating several sites of heat diffusion. Specimens tested along the printing direction revealed a classical fatigue behavior, i.e. with one dominating crack and localized plasticity and heat dissipation. This observation of the difference in damage and failure is a possible explanation for the different mean fatigue endurance limits. The transition points characterizing the switch from the primary to the secondary regime of the self-heating curves appear at higher stress amplitudes for the specimen tested perpendicular to the printing direction. Several important questions remain. What is the growth mechanism for the clusters of small grains? As well as their role in dissipating heat generated during mechanical testing and failure during cyclic loading? Being able to answer these questions would enable to: (i) an understanding of the crack initiation and (ii) lead to a better explanation of the crack arrest mechanisms in the case of the perpendicularly loaded specimens $A_{\perp}$.

Acknowledgement

The authors would like to thank Direction Général de l'Armement (DGA) for the funding of the BeAM *Mobile* machine used in this study. The FEG SEM FEI Quanta 600 has been acquired with the financial support of Region Ile-de-France (SESAME 2004 program), CNRS and École Polytechnique. The authors would also like to acknowledge the help of Lahcen Cherfa with the self-heating tests and Simon Hallais for the SEM measurements.

Figures and tables:

	$A_{\perp 0.12}$			$B_{/\!/ 0.2}$			$R_{0.12}$			$R_{0.2}$		
	All grains	*small* grains	*large* grains	All grains	*small* grains	*large* grains	All grains	*small* grains	*large* grains	All grains	*small* grains	*large* grains
Diameter average (μm)	26.6 ± 20.2	8.9 ± 3.6	35.2 ± 19.3	14.7 ± 14	7.2 ± 3.4	29.6 ± 15.3	25.2 ± 21.2	8.5 ± 3.5	36 ± 20.9	16.5 ± 15.6	7.6 ± 3.5	31 ± 16.8
Diameter median (μm)	22	96	29.9	9.8	6.5	24.4	19.3	8.4	29.5	11.2	7	25.5
Aspect ratio average	2.4 ± 1.3	2.3 ± 1.3	2.4 ± 1.2	2.7 ± 1.7	2.4 ± 2.4	3.3 ± 2	2.4 ± 1.3	2.3 ± 1.3	2.7 ± 1.6	2.4 ± 1.4	2.1 ± 1	2.9 ± 1.7
Aspect ratio median	2	2	2.1	2.2	2	2.8	2	2	2.2	2	1.8	2.4
Quantity of grains (%)		32.7	67.3		65.6	34.4		39.3	60.7		62.2	37.8
Surface occupied (%)		10.5	89.5		31.4	68.6		13.3	86.7		28.7	71.3
Surface of study (mm^2)	2.9×2.1			1.9×1.8			3.8×2			2.2×1.6		

Table 1: Grains size statistics.

Technology	σ_y (MPa)			UTS (MPa)			D (%)		
Printing versus tensile direction	$\perp$	$/\!/$	$r_{\frac{/\!/}{\perp}}$	$\perp$	$/\!/$	$r_{\frac{/\!/}{\perp}}$	$\perp$	$/\!/$	$r_{\frac{/\!/}{\perp}}$
$0.12\,mm$ configuration	445 ± 6.2	475 ± 5.3	1.06	639 ± 8.4	667 ± 11.4	1.05	51 ± 3.2	50 ± 3.8	0.98
$0.2\,mm$ configuration	420 ± 7.3	480 ± 8.5	1.14	597 ± 6.7	688 ± 10.3	1.15	46 ± 3.1	47 ± 4.2	1.02
$R_{0.12}$ configuration	418 ± 9.2	/	/	638 ± 7.6	/	/	45 ± 4.3	/	/
$R_{0.2}$ configuration	414 ± 6.7	/	/	602 ± 9.8	/	/	41 ± 3.6	/	/
Substrate	360 ± 14.5	/	/	660 ± 8.7	/	/	85 ± 8.1	/	/
316L - LENS [12] from bulk	479	576	1.2	703	776	1.1	46	33	0.72
316L LMDS [26] from wall	352	558	1.6	536	639	1.19	46	21	0.46
304L DED [55] from bulk	440	552	1.3	670	730	1.09	70	51	0.73

Table 2: Mechanical properties of 316L from the present tests and from the literature [12; 26; 55]. R is the ratio of the material parameters of the specimen $B_{/\!/}$ over the specimen $A_{\perp}$. In this table, bulk and wall stand for specimens extracted from multi-track thickness and single-track structures respectively.

Specimens	α	γ	m	Σ_∞	$r_{\Sigma_\infty \frac{0.12}{0.2}}$
$A_{\perp 0.12}$	0	2.84	5.58	373	1.08
$A_{\perp 0.2}$	0.28	2.38	10.59	345	
$B_{/\!/ 0.12}$	0	2.87	3.86	339	1.06
$B_{/\!/ 0.2}$	0	2.94	3.58	319	
$R_{0.12}$	0	2.08	2.6	293	1.13
$R_{0.2}$	0	1.13	3.24	259	
Substrate	0.17	2.54	6.22	328	/

Table 3: Values of the fitting parameters from Munier's model [38] and other relative values such as the mean endurance Σ_∞ and the ratio highlighting the effect of the vertical increment for a comparable configuration $r_{\Sigma_\infty \frac{0.12}{0.2}}$.

Specimens	$r_{\Sigma_\infty \frac{\perp}{/\!/}}$
$A_{\perp\, 0.12}$ $B_{/\!/\, 0.12}$	1.1
$A_{\perp\, 0.2}$ $B_{/\!/\, 0.2}$	1.08
$\perp$ [55]	> 1
$/\!/$ [55]	
$\perp$ [27]	1.07
$/\!/$ [27]	
$\perp$ [67]	1.17
$/\!/$ [67]	

Table 4: Anisotropic behavior of our specimens highlighted by the ratio of the mean endurance of the specimens perpendicular to the printing direction on the specimens parallel $r_{\Sigma_\infty \frac{\perp}{/\!/}}$. These values are compared with SS304 specimens manufactured by DED and WAAM in [55] and [27] respectively and also with SS316L specimens manufactured by SLM in [67]

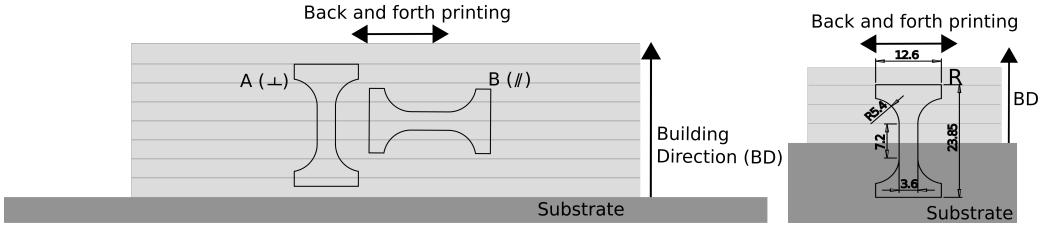

Figure 1: Schemes of the 316L single-track thickness walls where fully printed in both orientation and repaired specimens were extracted by water jet cutting. The common dimensions for all the specimens are presented on the scheme of the repaired specimens (right).

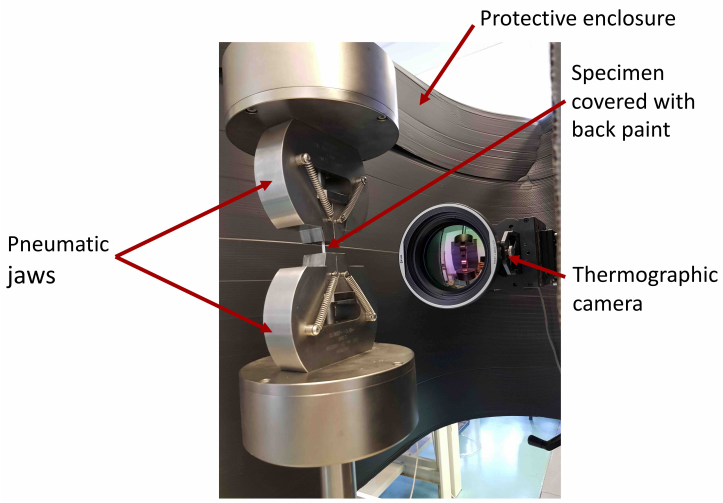

Figure 2: Experimental setup to measure the self-heating of the specimen during cyclic loadings.

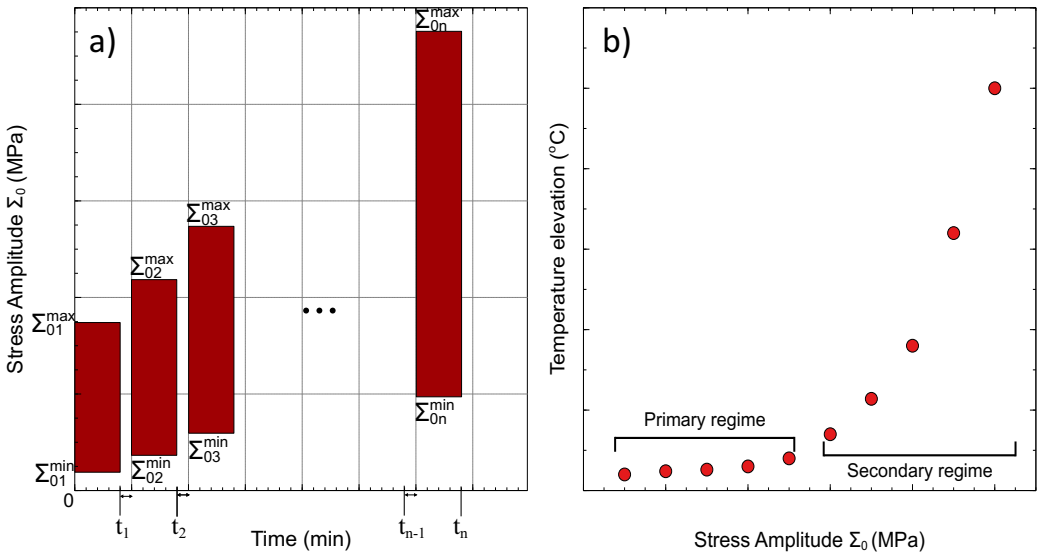

Figure 3: (a): (a) Successive series of cyclic loadings with increasing stress amplitudes Σ_0 for each block. The ratio of stress amplitude is constant throughout the whole test . Between the cyclic blocks, a hold time t_n in the elastic regime is performed to cool down the specimens. (b): Evolution of the temperature elevation during the self-heating test.

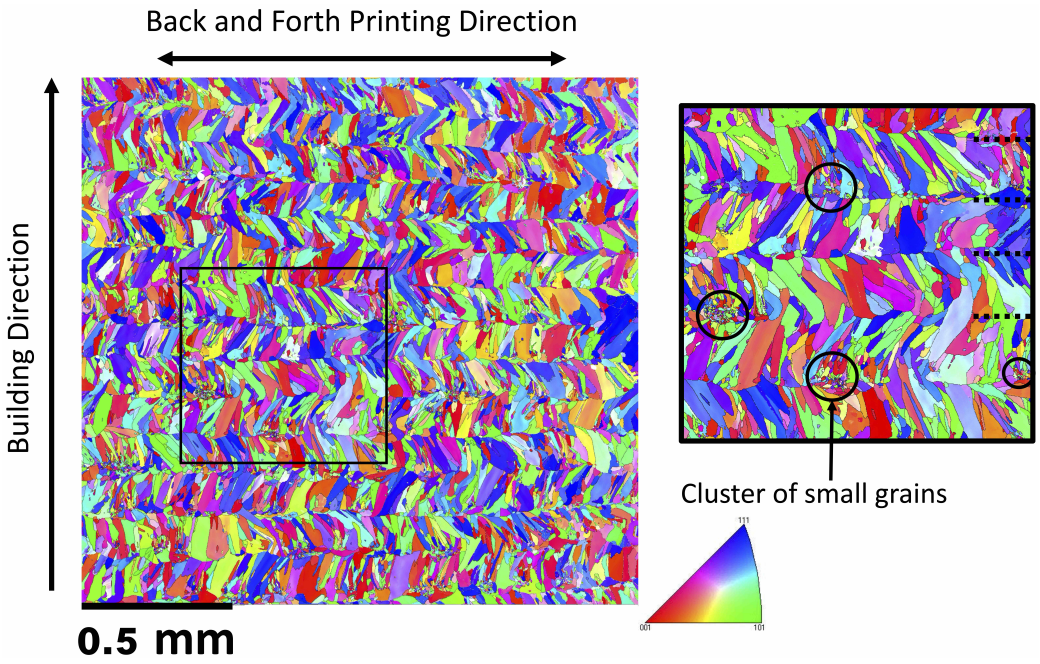

Figure 4: EBSD map (IPF along BD) of the specimen $B_{/\!/\,0.2}$. A zoomed-in portion to show in detail the microstructure and the presence of clusters of small grains between some layers.

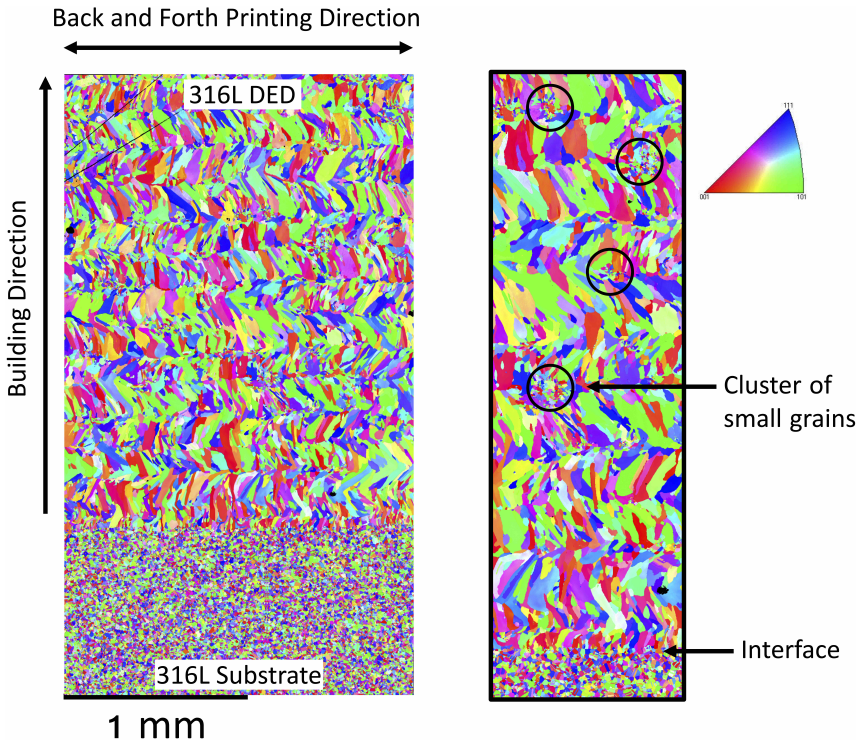

Figure 5: EBSD map (IPF along BD) of the specimen $R_{0.2}$. A zoomed-in portion to show in detail the zigzag pattern of the microstructure, the presence of clusters of small grains between some layers and the epitaxial growth from the substrate.

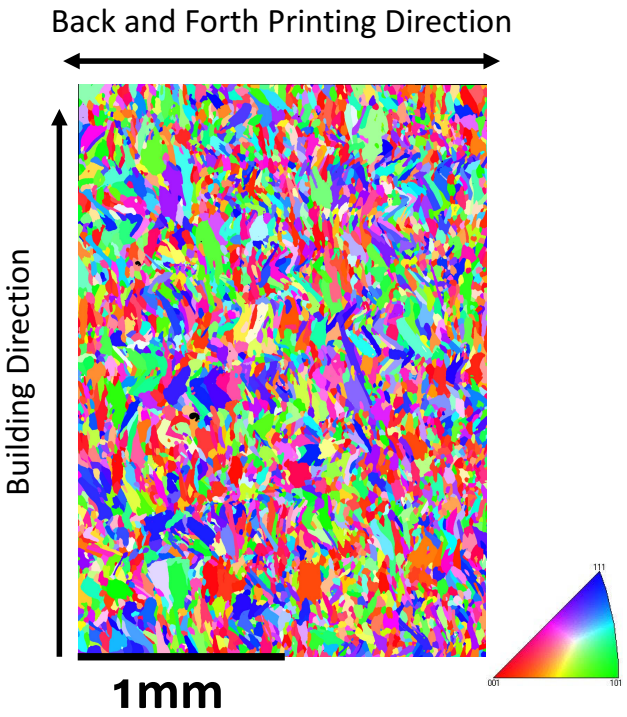

Figure 6: EBSD map (IPF along BD) of the specimen $A_{\perp\,0.12}$.

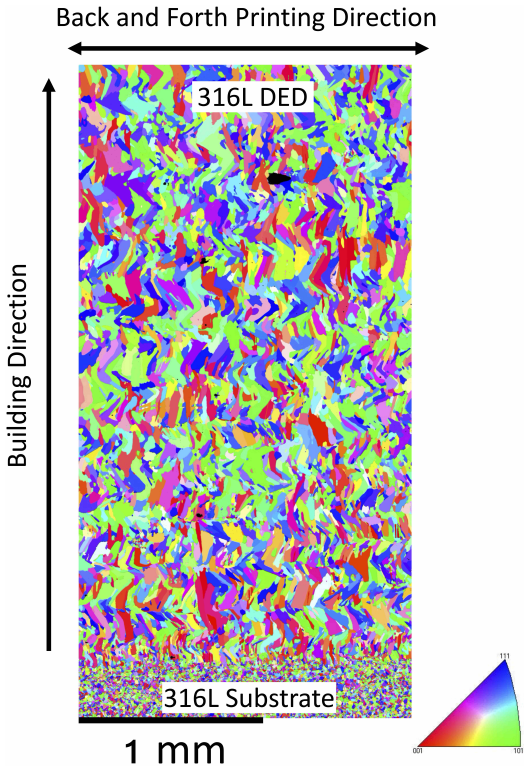

Figure 7: EBSD map (IPF along BD) of the specimen $R_{0.12}$ showing an epitaxial growth. The $R_{0.12}$ microstructure exhibits less of the zigzag pattern seen in the $R_{0.2}$ microstructure and a substantially reduced presence of the clusters of small grains at the interfaces between layers.

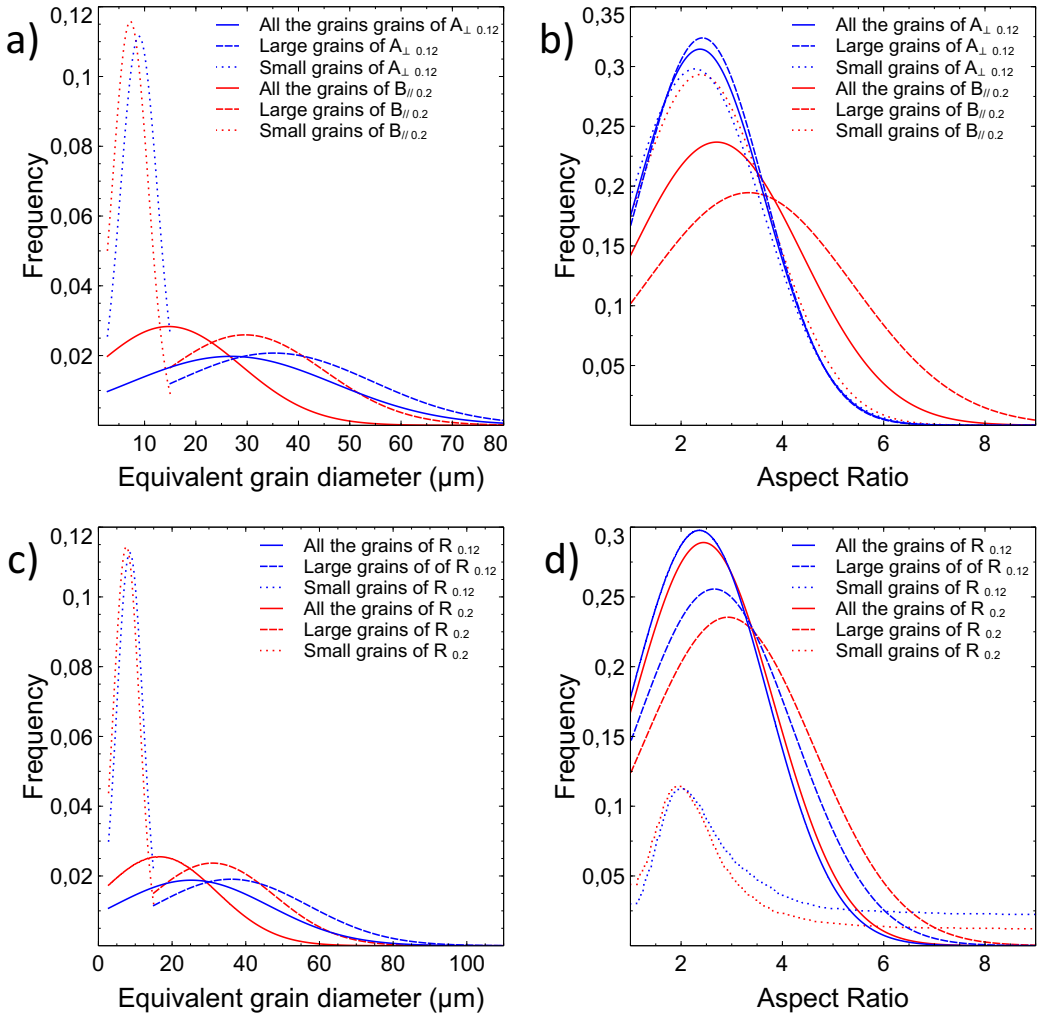

Figure 8: Probability density function of grain equivalent diameter, i.e. the diameter of a circle fitting the grain by its surface for the fully printed and repaired specimens in (a) and (c) respectively. Probability density function of grain ellipticity, i.e. frequency in terms of ratio between the large and small axes of the ellipse fitting the grain by its surface and shape in (b) and (d) respectively.

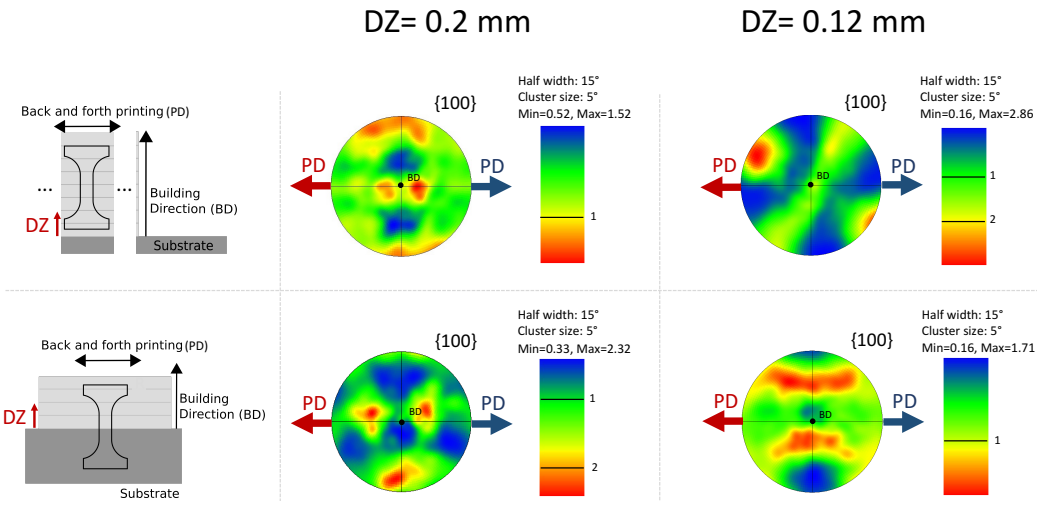

Figure 9: Pole figures of the crystallographic texture of the fully printed and repaired specimens with respect to their vertical increment.

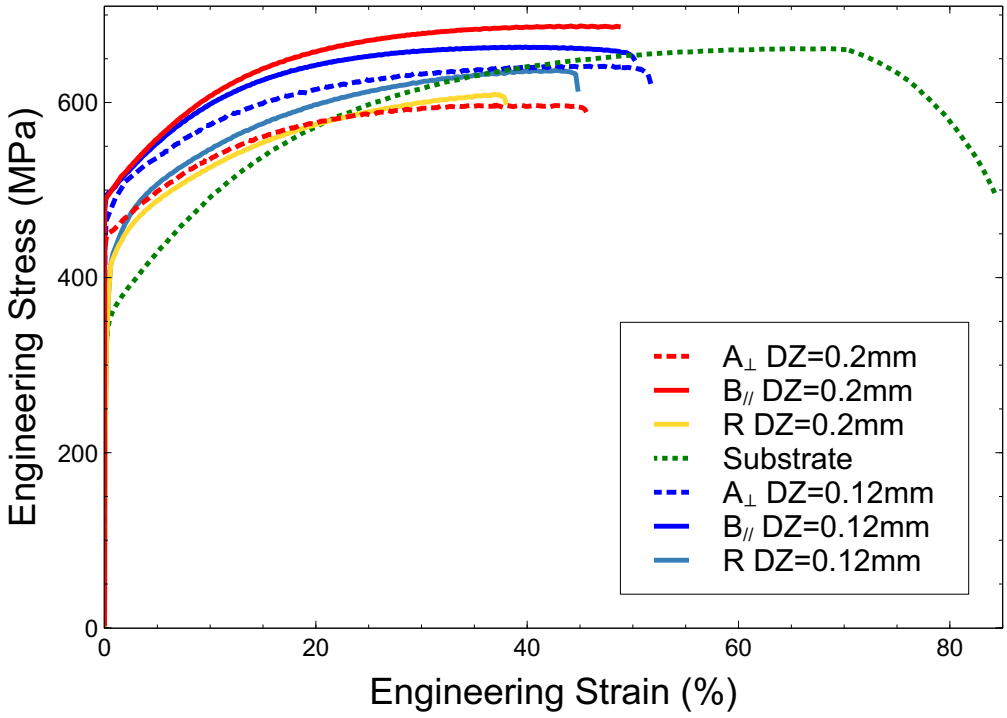

Figure 10: Tensile stress-strain curves of all the specimens.

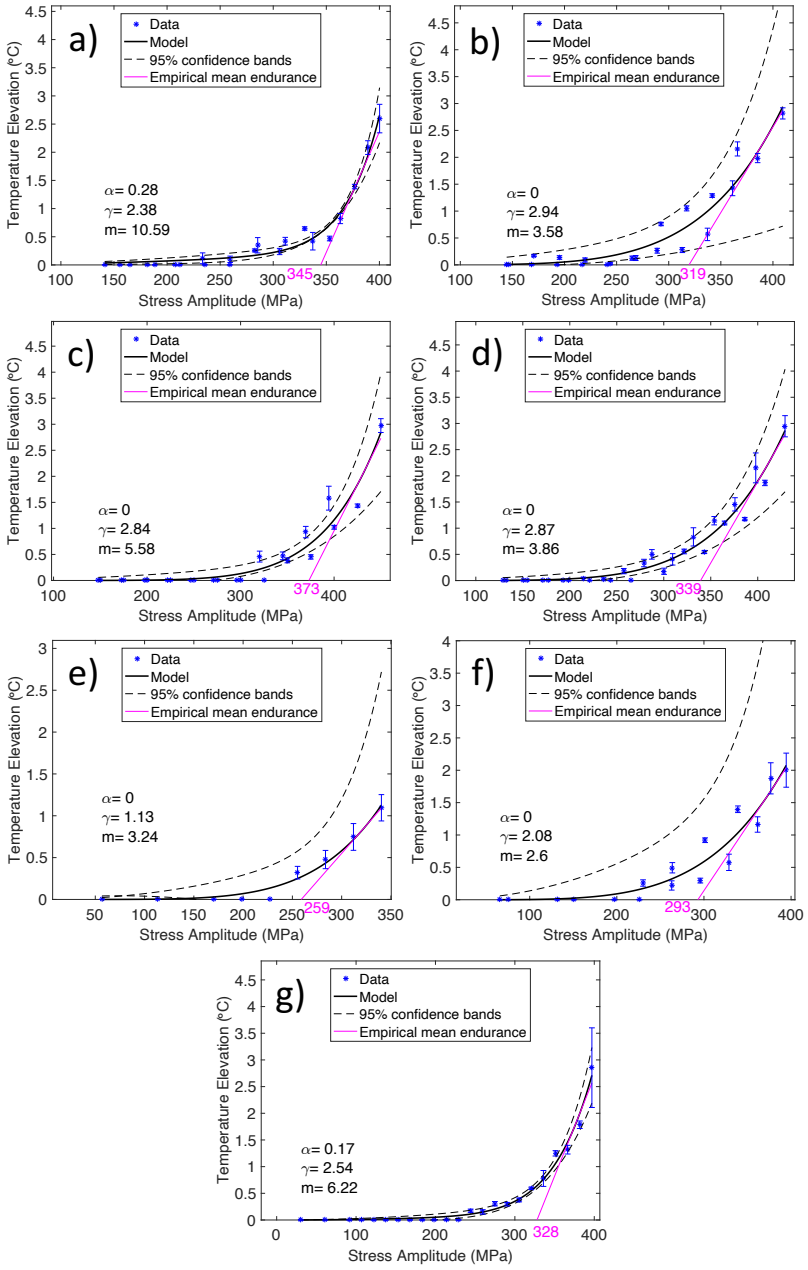

Figure 11: Evolution of the temperature elevation of the specimen associated with a level of stress amplitude for specimens $A_{\perp\,0.2}$, $B_{/\!/\,0.2}$, $A_{\perp\,0.12}$, $B_{/\!/\,0.12}$, $R_{0.2}$, $R_{0.12}$ and the substrate in (a), (b), (c), (d), (e), (f) and (g) respectively. A self-heating model proposed in [38] is fitted on the experimental data and used to determine the mean endurance limit (pink). The coefficients of the models and the mean endurances are listed in table 3.

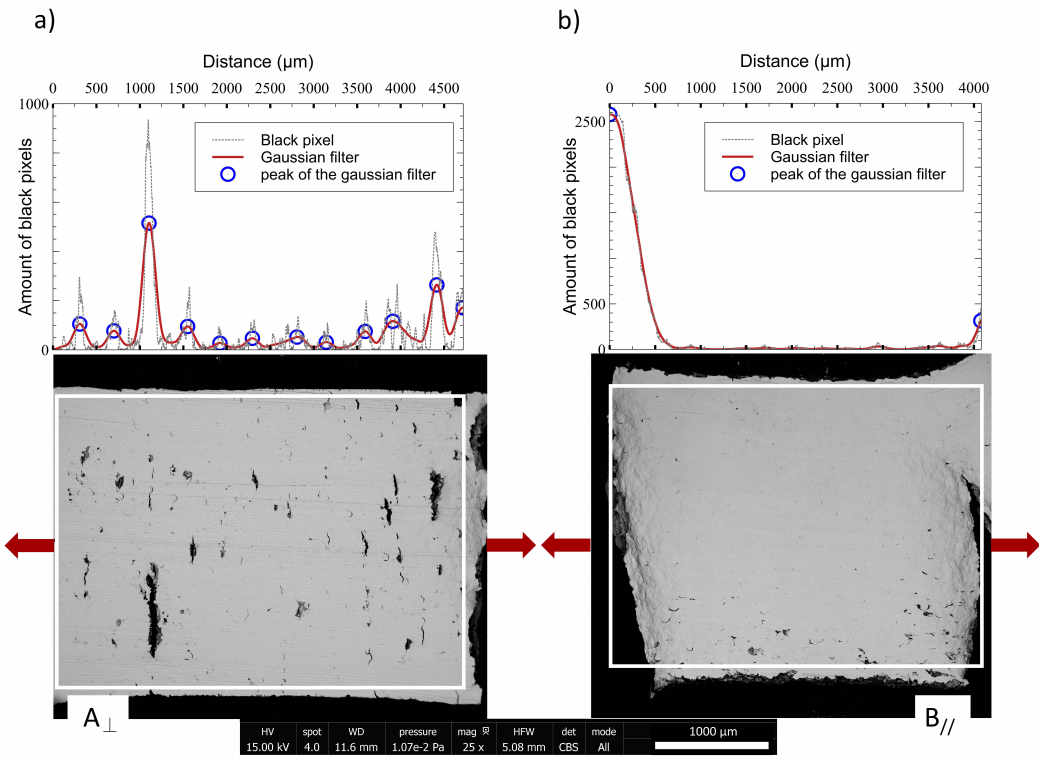

Figure 12: Self-heating test post mortem SEM images for specimens $A_{\perp}$ and $B_{/\!/}$ in (a) and (b) respectively. The lower portions of the figures are the actual SEM images from which one can distinguish two distinct patterns for the onset of crack initiation sites. The tensile loading direction is indicated by the red arrows. The upper portions of the figures are the sum of the black pixels for each vertical line of the SEM images. The maximum values obtained after Moving Average filtering and determination of the local maxima correspond to the location of the cracks

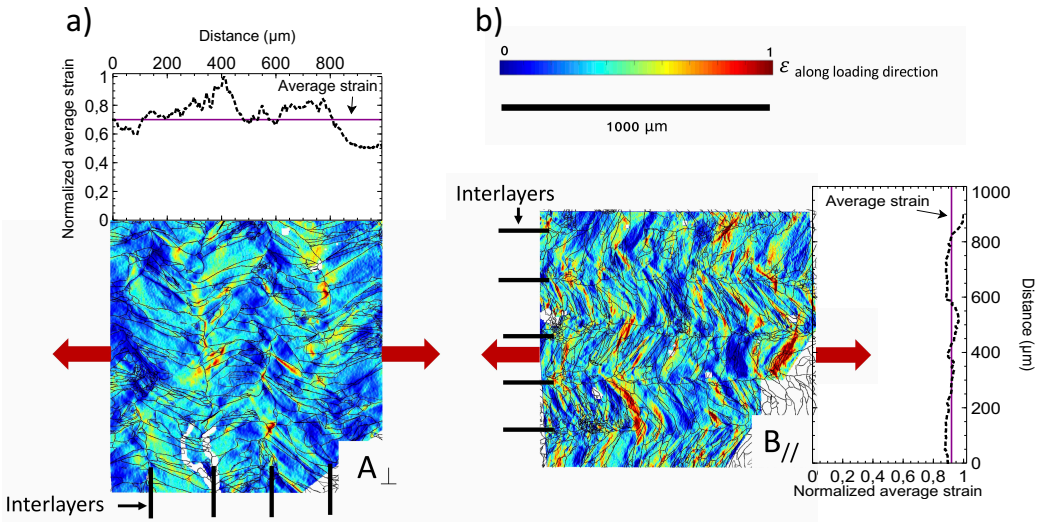

Figure 13: Strain localization along the loading direction, indicated by the red arrows, for specimens $A_{\perp}$ and $B_{/\!/}$ in (a) and (b) respectively. The strain is heterogeneously distributed for $A_{\perp}$ with localization occurring at some interfaces. For $B_{/\!/}$, the strain is more homogeneously distributed. The complete experiment and results are available in [11]

Bibliography:

[1] Olga Vayena, Charalabos Doumanidis, Rajesh Ranganathan, and Teiichi Ando. Welding methods for production of mmc coatings using particulate-cored wire precursors. *Journal of Manufacturing Processes*, 7(2):130 – 139, 2005.

[2] M.F. Morks, N.F. Fahim, and A. Kobayashi. Microstructure, corrosion behavior, and microhardness of plasma-sprayed w–ni composite coatings. *Journal of Manufacturing Processes*, 10(1):6 – 11, 2008.

[3] R.G. Bonora, H.J.C. Voorwald, M.O.H. Cioffi, G.S. Junior, and L.F.V. Santos. Fatigue in aisi 4340 steel thermal spray coating by hvof for aeronautic application. *Procedia Engineering*, 2(1):1617 – 1623, 2010. Fatigue 2010.

[4] W. Kaysser. Surface modifications in aerospace applications. *Surface Engineering*, 17(4):305–312, 2001.

[5] Shuo Yin, Pasquale Cavaliere, Barry Aldwell, Richard Jenkins, Hanlin Liao, Wenya Li, and Rocco Lupoi. Cold spray additive manufacturing and repair: Fundamentals and applications. *Additive Manufacturing*, 21:628 – 650, 2018.

[6] International Organization for Standardization. Iso/astm 52900, additive manufacturing - general principles - terminology. Technical report, ASTM International, 2015.

[7] MyoungGuk Park, SeJin Ahn, Jae Ho Yun, Jihye Gwak, Ara Cho, SeoungKyu Ahn, Keeshik Shin, Dahyun Nam, Hyeonsik Cheong, and Kyunghoon Yoon. Characteristics of cu(in,ga)se2 (cigs) thin films deposited by a direct solution coating process. *Journal of Alloys and Compounds*, 513:68 – 74, 2012.

[8] A J Pinkerton, W Wang, and L Li. Component repair using laser direct metal deposition. *Proceedings of the Institution of Mechanical Engineers, Part B: Journal of Engineering Manufacture*, 222(7):827–836, 2008.

[9] J. Michael Wilson, Cecil Piya, Yung C. Shin, Fu Zhao, and Karthik Ramani. Remanufacturing of turbine blades by laser direct deposition

with its energy and environmental impact analysis. *Journal of Cleaner Production*, 80:170 – 178, 2014.

[10] Chunlei Qiu, Sheng Yue, Nicholas J.E. Adkins, Mark Ward, Hany Hassanin, Peter D. Lee, Philip J. Withers, and Moataz M. Attallah. Influence of processing conditions on strut structure and compressive properties of cellular lattice structures fabricated by selective laser melting. *Materials Science and Engineering: A*, 628:188 – 197, 2015.

[11] Eric Charkaluk Yanis Balit and Andrei Constantinescu. Digital image correlation for microstructural analysis of deformation pattern in additively manufactured 316l thin walls. *Additive Manufacturing*, sent to production 07/09/2019.

[12] Michał Ziętala, Tomasz Durejko, Marek Polanski, Izabela Kunce, Tomasz Płociński, Witold Zieliński, Magdalena Łazińska, Wojciech Stłepniowski, Tomasz Czujko, K.J. Kurzydłowski, and Zbigniew Bojar. The microstructure, mechanical properties and corrosion resistance of 316l stainless steel fabricated using laser engineered net shaping. *Materials Science and Engineering: A*, 677:1–10, 11 2016.

[13] J. Nguejio, F. Szmytka, S. Hallais, A. Tanguy, S. Nardone, and M. Godino Martinez. Comparison of microstructure features and mechanical properties for additive manufactured and wrought nickel alloys 625. *Materials Science and Engineering: A*, 764:138214, 2019.

[14] J. Leunda, C. Soriano, C. Sanz, and V. García Navas. Laser cladding of vanadium-carbide tool steels for die repair. *Physics Procedia*, 12:345 – 352, 2011. Lasers in Manufacturing 2011 - Proceedings of the Sixth International WLT Conference on Lasers in Manufacturing.

[15] Y.T Pei and J.Th.M De Hosson. Functionally graded materials produced by laser cladding. *Acta Materialia*, 48(10):2617 – 2624, 2000.

[16] X. Lin, T.M. Yue, H.O. Yang, and W.D. Huang. Laser rapid forming of ss316l/rene88dt graded material. *Materials Science and Engineering: A*, 391(1):325 – 336, 2005.

[17] S. Mokadem, C. Bezençon, A. Hauert, A. Jacot, and W. Kurz. Laser repair of superalloy single crystals with varying substrate orientations. *Metallurgical and Materials Transactions A*, 38(7):1500–1510, Jul 2007.

[18] H. Paydas, A. Mertens, R. Carrus, J. Lecomte-Beckers, and J. Tchoufang Tchuindjang. Laser cladding as repair technology for ti–6al–4v alloy: Influence of building strategy on microstructure and hardness. *Materials & Design*, 85:497 – 510, 2015.

[19] Jae-Hyun Yu, Yoon-Suk Choi, Do-Sik Shim, and Sang-Hu Park. Repairing casting part using laser assisted additive metal-layer deposition and its mechanical properties. *Optics & Laser Technology*, 106:87 – 93, 2018.

[20] Wook Jin Oh, Wook Jin Lee, Min Seob Kim, Jong Bae Jeon, and Do Sik Shim. Repairing additive-manufactured 316l stainless steel using direct energy deposition. *Optics & Laser Technology*, 117:6 – 17, 2019.

[21] Bonny Onuike and Amit Bandyopadhyay. Additive manufacturing in repair: Influence of processing parameters on properties of inconel 718. *Materials Letters*, 252:256 – 259, 2019.

[22] A. Constantinescu, K. Dang van, and M. H. Maitournam. A unified approach for high and low cycle fatigue based on shakedown concepts. *Fatigue & Fracture of Engineering Materials & Structures*, 26(6):561–568, 2003.

[23] Vincent Monchiet, Eric Charkaluk, and Djimedo Kondo. Plasticity-damage based micromechanical modelling in high cycle fatigue. *Comptes Rendus Mécanique*, 334(2):129–136, 2006.

[24] Aref Yadollahi and Nima Shamsaei. Additive manufacturing of fatigue resistant materials: Challenges and opportunities. *International Journal of Fatigue*, 98:14 – 31, 2017.

[25] Todd M. Mower and Michael J. Long. Mechanical behavior of additive manufactured, powder-bed laser-fused materials. *Materials Science and Engineering: A*, 651:198 – 213, 2016.

[26] Kai Zhang, Shijie Wang, Weijun Liu, and Xiaofeng Shang. Characterization of stainless steel parts by laser metal deposition shaping. *Materials and Design*, 55:104 – 119, 2014.

[27] Jerard Gordon, Jacob Hochhalter, Christina Haden, and D. Gary Harlow. Enhancement in fatigue performance of metastable austenitic stainless steel through directed energy deposition additive manufacturing. *Materials & Design*, 168:107630, 2019.

[28] Shi Da Sun, Qianchu Liu, Milan Brandt, Vladimir Luzin, Ryan Cottam, Madabhushi Janardhana, and Graham Clark. Effect of laser clad repair on the fatigue behaviour of ultra-high strength aisi 4340 steel. *Materials Science and Engineering: A*, 606:46 – 57, 2014.

[29] Yi Rye Choi, Shi D Sun, Qianchu Liu, Milan Brandt, and Ma Qian. Influence of deposition strategy on the microstructure and fatigue properties of laser metal deposited ti-6al-4v powder on ti-6al-4v substrate. *International Journal of Fatigue*, page 105236, 2019.

[30] C. E. Stromeyer and William Ernest Dalby. The determination of fatigue limits under alternating stress conditions. *Proceedings of the Royal Society of London. Series A, Containing Papers of a Mathematical and Physical Character*, 90(620):411–425, 1914.

[31] Cédric Doudard and Sylvain Calloch. Influence of hardening type on self-heating of metallic materials under cyclic loadings at low amplitude. *European Journal of Mechanics - A/Solids*, 28(2):233 – 240, 2009.

[32] Anthony Ezanno, Cédric Doudard, Sylvain Calloch, and Jean-Loup Heuzé. A new approach to characterizing and modeling the high cycle fatigue properties of cast materials based on self-heating measurements under cyclic loadings. *International Journal of Fatigue*, 47:232 – 243, 2013.

[33] C. Doudard, M. Poncelet, S. Calloch, C. Boue, F. Hild, and A. Galtier. Determination of an hcf criterion by thermal measurements under biaxial cyclic loading. *International Journal of Fatigue*, 29(4):748 – 757, 2007.

[34] L. Zhang, X.S. Liu, S.H. Wu, Z.Q. Ma, and H.Y. Fang. Rapid determination of fatigue life based on temperature evolution. *International Journal of Fatigue*, 54:1 – 6, 2013.

[35] Eric Charkaluk and Andrei Constantinescu. Dissipative aspects in high cycle fatigue. *Mechanics of Materials*, 41(5):483 – 494, 2009.

[36] Etienne Pessard, Franck Morel, Catherine Verdu, Laurent Flacelière, and Gilles Baudry. Microstructural heterogeneities and fatigue anisotropy of forged steels. *Materials Science and Engineering: A*, 529:289 – 299, 2011.

[37] Charles Mareau, Véronique Favier, Bastien Weber, André Galtier, and Marcel Berveiller. Micromechanical modeling of the interactions between the microstructure and the dissipative deformation mechanisms in steels under cyclic loading. *International Journal of Plasticity*, 32-33:106 – 120, 2012.

[38] Rémi Munier, Cédric Doudard, Sylvain Calloch, and Bastien Weber. Determination of high cycle fatigue properties of a wide range of steel sheet grades from self-heating measurements. *International Journal of Fatigue*, 63:46 – 61, 2014.

[39] www.flowwaterjet.com.

[40] www.hoganas.com.

[41] www.beam-machines.com.

[42] Balit Y., Durbecq S., Charkaluk E. and Constantinescu A., Microstructure and process parameters for directed energy deposition additive manufacturing. *The Romanian Journal of Technical Sciences - Applied Mechanics*, 2019.

[43] https://www.instron.com.

[44] L. Allais, M. Bornert, T. Bretheau, and D. Caldemaison. Experimental characterization of the local strain field in a heterogeneous elastoplastic material. *Acta Metallurgica et Materialia*, 42(11):3865 – 3880, 1994.

[45] Michel Bornert, F. Vales, H. Gharbi, and D. Nguyen Minh. Multiscale Full-Field Strain Measurements for Micromechanical Investigations of the Hydromechanical Behaviour of Clayey Rocks. *Strain*, 46(1):33–46, 2010.

[46] www.flir.com.

[47] M.P. Luong. Infrared thermographic scanning of fatigue in metals. *Nuclear Engineering and Design*, 158(2):363 – 376, 1995.

[48] Cédric Doudard, Sylvain Calloch, François Hild, and Stéphane Roux. Identification of heat source fields from infrared thermography: Determination of 'self-heating' in a dual-phase steel by using a dog bone sample. *Mechanics of Materials*, 42(1):55 – 62, 2010.

[49] Lakshmi L. Parimi, G.A. Ravi, Daniel Clark, and Moataz M. Attallah. Microstructural and texture development in direct laser fabricated IN718. *Materials Characterization*, 89:102–111, 2014.

[50] G. P. Dinda, A. K. Dasgupta, and J. Mazumder. Laser aided direct metal deposition of Inconel 625 superalloy: Microstructural evolution and thermal stability. *Materials Science and Engineering A*, 509(1-2):98–104, 2009.

[51] H L Wei, J Mazumder, and T DebRoy. Evolution of solidification texture during additive manufacturing. *Sci Rep*, 5:16446, Nov 2015.

[52] Hasse Fredriksson and Ulla Åkerlind. *Solidification and Crystalisation Processing in Metals and Alloys*. John Wiley & Sons, 01 2012.

[53] Xin Zhou, Kailun Li, Dandan Zhang, Xihe Liu, Jing Ma, Wei Liu, and Zhijian Shen. Textures formed in a cocrmo alloy by selective laser melting. *Journal of Alloys and Compounds*, 631:153 – 164, 2015.

[54] Olivier Andreau, Imade Koutiri, Patrice Peyre, Jean-Daniel Penot, Nicolas Saintier, Etienne Pessard, Thibaut De Terris, Corinne Dupuy, and Thierry Baudin. Texture control of 316l parts by modulation of the melt pool morphology in selective laser melting. *Journal of Materials Processing Technology*, 264:21 – 31, 2019.

[55] Thale R Smith, Joshua D Sugar, Chris San Marchi, and Julie M Schoenung. Orientation Effects on Fatigue Behavior of Additively Manufactured Stainless Steel, 2017.

[56] J. Yu, M. Rombouts, and G. Maes. Cracking behavior and mechanical properties of austenitic stainless steel parts produced by laser metal deposition. *Materials and Design*, 45:228 – 235, 2013.

[57] M.L. Griffith, D.M. Keicher, and J.T. Atwood. Free form fabrication of metallic components using laser engineering net shaping (lens). *Proceedings of the Solid Freeform Fabrication Symposium*, pages 125–132, 1996. cited By 1.

[58] Zhuqing Wang, Todd A. Palmer, and Allison M. Beese. Effect of processing parameters on microstructure and tensile properties of austenitic stainless steel 304L made by directed energy deposition additive manufacturing. *Acta Materialia*, 110:226–235, 2016.

[59] T. DebRoy, H.L. Wei, J.S. Zuback, T. Mukherjee, J.W. Elmer, J.O. Milewski, A.M. Beese, A. Wilson-Heid, A. De, and W. Zhang. Additive manufacturing of metallic components – process, structure and properties. *Progress in Materials Science*, 92:112 – 224, 2018.

[60] Jorge Jorge. Influence of chemical composition on the mechanical properties of high strength steel weld metals for application in mooring components. *International Journal of Engineering and Technical Research*, 4:71–76, 02 2016.

[61] J.E. MacDonald, R.H.U. Khan, M. Aristizabal, K.E.A. Essa, M.J. Lunt, and M.M. Attallah. Influence of powder characteristics on the microstructure and mechanical properties of hipped cm247lc ni superalloy. *Materials & Design*, 174:107796, 2019.

[62] Yanyan Zhu, Jia Li, Xiangjun Tian, Huaming Wang, and Dong Liu. Microstructure and mechanical properties of hybrid fabricated ti–6.5al–3.5mo–1.5zr–0.3si titanium alloy by laser additive manufacturing. *Materials Science and Engineering: A*, 607:427 – 434, 2014.

[63] Zhuang Zhao, Jing Chen, Hua Tan, Xin Lin, and Weidong Huang. Evolution of plastic deformation and its effect on mechanical properties of laser additive repaired ti64eli titanium alloy. *Optics & Laser Technology*, 92:36 – 43, 2017.

[64] Pierrick Florin, Matteo Facchinetti, Cédric Doudard, and Sylvain Calloch. Fast fatigue properties identification by "self-heating" method: Application to automotive welded joints. *Procedia Engineering*, 66:676 – 683, 2013. Fatigue Design 2013, International Conference Proceedings.

[65] Catherine Peyrac, Thomas Jollivet, Nolwenn Leray, Fabien Lefebvre, Ophélie Westphal, and Laurent Gornet. Self-heating method for fatigue limit determination on thermoplastic composites. *Procedia Engineering*, 133:129 – 135, 2015. Fatigue Design 2015, International Conference Proceedings, 6th Edition.

[66] Parham Mostofizadeh, Mahmoud Kadkhodaei, Shabnam Arbab Chirani, Luc Saint-Sulpice, Maha Rokbani, Tarak Bouraoui, and Sylvain Calloch. Fatigue analysis of shape memory alloys by self-heating method. *International Journal of Mechanical Sciences*, 156:329 – 341, 2019.

[67] Bastian Blinn, Maximilian Ley, Nils Buschhorn, Roman Teutsch, and Tilmann Beck. Investigation of the anisotropic fatigue behavior of additively manufactured structures made of aisi 316l with short-time procedures phyballit and phybalcht. *International Journal of Fatigue*, 124:389 – 399, 2019.

[68] A. Riemer, S. Leuders, M. Thöne, H.A. Richard, T. Tröster, and T. Niendorf. On the fatigue crack growth behavior in 316l stainless steel manufactured by selective laser melting. *Engineering Fracture Mechanics*, 120:15 – 25, 2014.

[69] J.V. Gordon, C.V. Haden, H.F. Nied, R.P. Vinci, and D.G. Harlow. Fatigue crack growth anisotropy, texture and residual stress in austenitic steel made by wire and arc additive manufacturing. *Materials Science and Engineering: A*, 724:431 – 438, 2018.

[70] Nicolas Malésys, Ludovic Vincent, and François Hild. A probabilistic model to predict the formation and propagation of crack networks in thermal fatigue. *International Journal of Fatigue*, 31(3):565 – 574, 2009.